Gaussian Beam Migration for Wide-Area Deep Ocean Floor Mapping

A. Charous[a], W.H. Ali[a], P. Ryu[b], D. Brown[b], K. Arsenault[b],
B. Cho[b], K. Rimpau[b], A. March[b], P.F.J. Lermusiaux[a*]

[a]Department of Mechanical Engineering, Center for Computational Science and Engineering,
Massachusetts Institute of Technology, Cambridge, MA 02139, USA;
[b]Advanced Undersea Systems and Technology Group,
MIT Lincoln Laboratory, Lexington, MA 02421, USA;
*Corresponding Author: pierrel@mit.edu

***Abstract*—Cost-effective seafloor mapping at high resolution is yet to be attained. A possible solution consists of using a mobile, wide-aperture, sparse array with subarrays distributed across multiple autonomous surface vessels. Such wide-area mapping with multiple dynamic sources and receivers require accurate modeling and processing systems for imaging the seabed. In this paper, we focus on computational schemes and challenges for such high-resolution acoustic imaging or migration. Starting from the imaging condition from the adjoint-state method, we derive a closed-form expression for Gaussian beam migration in stratified media. We employ this technique on simulated data and on real data collected with our novel acoustic array over shipwrecks in the Boston Harbor. We compare Gaussian beam migration with diffraction stack and Kirchhoff migration, and we find that Gaussian beam migration produces the clearest images with the fewest artifacts.**

I. Introduction

Mapping the seafloor remains a tremendous challenge. The average depth of the ocean is 3.7 km, but no technology exists to obtain meter-scale resolution maps of the ocean with water deeper than 1 km [1–4]. Developing a large-scale high-resolution mapping system may enable safe navigation for submersibles, monitoring of critical infrastructure, locating missing objects, as well as identifying and tracking of hazardous geological processes and vulnerable ecosystems and habitats [5–7]. Recently, we proposed and tested a cost-effective technology to obtain high-resolution and rapid seafloor mapping in deep water with a custom acoustic array [8]. Our design concept uses a mobile, wide-aperture, sparse array with subarrays distributed across multiple autonomous surface vessels, each hosting a small local sonar array.

The most basic algorithm of active sonar is to emit a pulse and record the time it takes to propagate through the water, reflect off of the seafloor, and return to a hydrophone. This would provide an estimate of the bathymetry. But, this is insufficient to map wide areas of the ocean since it only provides a one-dimensional (1D) representation of the ocean per ping, and it ignores acoustic reflections generated by layered media. By including multiple acoustic sources and receivers, we can not only estimate the depth of the seafloor, but provide a three-dimensional (3D) representation of acoustic scatterers in the ocean. However, imaging the seafloor across a large aperture using a dense array of transmitters and receivers comes with prohibitive costs. In addition, the acoustic data recorded are inherently noisy and high-dimensional. To address these challenges, our wide-area deep ocean floor mapping system proposed in [8] synthesizes a large effective array aperture using a sparsely populated 2D array of dynamic transmitters and receivers. The system additionally consists of a signal processing chain where the array data are conditioned using matched filtering and calibration for the image reconstruction step. In this work, we focus on this latter step of imaging, also known as migration, where our goal is to develop a robust, highly efficient algorithm that generates 3D images of objects in the ocean.

Mapping the ocean floor can be broadly defined as a depth migration task where the goal is to locate the acoustic scatterers in the ocean-seabed environment and construct a map of all reflecting interfaces. Depth migration algorithms are classified as ray-based and wave equation-based methods. Ray-based methods such as diffraction stack [9], Kirchhoff migration [10, 11], and beam migration methods [12, 13], have been used for seismic imaging due to their efficiency and ease-of-use [14]. However, some limitations arise due to their high-frequency asymptotic assumptions restricting their use to simplified environments and coarser resolutions [14]. On the other hand, wave-equation-based methods such as downward continuation and reverse-time/adjoint-based methods emanate from solutions of the acoustic wave equation and have emerged as the methods of choice for full-waveform inversion and imaging [14–16]. Adjoint-based methods in particular are desirable for imaging due to their efficiency in solving the least-squares optimization problem that minimizes the misfit between observed and computed data [17–19]. The optimization of the misfit cost function then allows for the determination of the model parameters, which, in the case of imaging, corresponds to the location and amplitude of

979-8-218-14218-6 ©2023 MTS

the acoustic scatterers using measured data. These advantages led to widespread applications of adjoint-based methods for imaging and inversion in inverse scattering [20, 21], seismology [17, 18, 22], and electromagnetic tomography [23, 24]. In addition to their use for wave-based inversion, adjoint-based methods have also been prominent in ocean science [25–27] and atmospheric science [28–30]. In the context of ocean acoustics, adjoint-state methods have been used for ocean acoustic tomography [31–33], geoacoustic inversion [34–37], and for optimal control for underwater acoustic sensing [38, 39, & references therein].

In this work, we extend the adjoint-state imaging methods for applications in ocean floor mapping. We start from the least-squares optimization problem for minimizing the misfit between our array's time-series data and the computed time-series from the full acoustic wave equation. Imaging the seafloor is then presented in terms of the so-called imaging condition [16, 40]. A common challenge in adjoint-state methods and the imaging condition is the requirement to compute and store the forward and adjoint fields [19]. Our approach facilitates this computation by deriving a closed-form expression for the forward and adjoint fields in stratified ocean environments using the narrow-angle parabolic equation initialized with Gaussian beams [41, 42]. In addition, we parallelize our implementation of this closed-form Gaussian beam migration algorithm and use GPUs to gain a computational speedup of $> 450\times$, making it suitable for imaging the seafloor using our sparse array in quasi-real-time.

We structure the paper as follows. In section II, we summarize the optimization problem and the imaging condition. We then make a parabolic approximation to the Green's function of the Helmholtz equation to obtain our Gaussian beam migration algorithm. In section III, to compare with Gaussian beam migration, we write out common ray-based acoustic inversion techniques used in acoustic, seismic, and electromagnetic wave imaging: diffraction stack [9] and Kirchhoff migration [10, 11, 14]. In section IV, we apply and evaluate our algorithm on simulated data as well as real data collected at sea in the Boston Harbor with our acoustic array. Finally, we conclude in section V with closing remarks and future research directions.

II. Gaussian Beam Adjoint-State Method

The goal of this section is to derive a closed-form expression to form 3D images of acoustic scatterers. First, we discuss the physics and mathematical formulation of the problem.

Acoustical phenomena are governed by the wave equation,

$$\frac{1}{c^2}\frac{\partial^2}{\partial t^2}u - \nabla^2 u = f,$$

where c denotes the sound speed, u is the acoustic pressure, and f is some forcing. The Helmholtz equation may be derived by Fourier-transforming the wave equation in time, giving

$$\nabla^2 \hat{u} + k^2 \hat{u} = -\hat{f},$$

where $\hat{u}$ denotes the Fourier-transformed acoustic pressure, $k = \omega/c$ is the wavenumber, ω is the angular frequency, and $\hat{f}$ is the Fourier-transformed forcing. For this paper, we operate in the frequency domain due to the parallelizability of the forthcoming algorithm. Scattering of the wavefield occurs due to discontinuities in the acoustic media, i.e. in c or k. We call these discontinuities "scatterers," and the goal of imaging is to locate scatterers from their reflections.

Let $\mathcal{F} : m \to d$ denote a mapping between the model of our system we are trying to invert, in this case, the slowness $m = 1/c^2$, and the data we observe, d, which are acoustic reflections recorded by hydrophones. $\mathcal{F}$ may be thought of as the forward operator that, given the environmental model slowness field m, returns the wavefield governed by the wave equation at receiver locations. To invert this operator, the optimization problem we seek to solve is

$$\arg\min_m \|\mathcal{F}[m] - d\|_2.$$

The adjoint-state method is a way to efficiently evaluate the gradient of the cost function in the minimization problem above. We refer to [18, 43] for a review of the adjoint-state method, and we recommend [40] for a derivation of the imaging condition given below, which amounts to performing one step of gradient descent and is often called reverse-time migration (RTM). Let F^* denote the adjoint of the linearization of $\mathcal{F}$ and δm denote a perturbation in the slowness (i.e., the scatterers). In the frequency domain, we have that

$$\begin{aligned}\delta m(x,y,z) &\propto (F^* d)(x,y,z)\\ &= 2\pi \int \hat{q}(x,y,z,\omega)\omega^2 \overline{\hat{u}_0(x,y,z,\omega)} d\omega, \quad (1)\\ \hat{q}(x,y,z,\omega) &= \int \overline{\hat{G}(\acute{x},\acute{y},\acute{z},x,y,z,\omega)} \cdot \\ &\qquad \hat{d}_{\text{ext}}(\acute{x},\acute{y},\acute{z},\omega) d\acute{x} d\acute{y} d\acute{z}. \quad (2)\end{aligned}$$

Variables with $\bar{}$ are complex conjugated and $\hat{}$ are Fourier-transformed. $\hat{q}$ is adjoint field, $\hat{G}$ is the Green's function of the Helmholtz equation, and $\hat{u}_0$ is the solution to the Helmholtz equation given an initial guess for the slowness m_0, implying that $m \approx m_0 + \delta m$. $\hat{d}_{\text{ext}}$ are the *extended* data expressed as a field by

$$\hat{d}_{\text{ext}}(x,y,z,\omega) = \sum_j \hat{d}_j(\omega)\delta(x - x_j)\delta(y - y_j)\delta(z - z_j),$$

where $\hat{d}_j$ are individual data streams for each j receiver at position (x_j, y_j, z_j), and δ is the Dirac delta function.

With equations (1) and (2), we have a way to obtain an approximate 3D image of the scatterers δm given hydrophone data d. As an approximation to the Green's function of the Helmholtz equation $\hat{G}$, one may use Gaussian beams [44–47], which are an exact solution of the parabolic wave equation [42], a one-way equation often used to approximate solution to the Helmholtz equation in weakly scattering media. Such an approximation is often made due to the computational difficulty in solving the Helmholtz equation; in contrast, Gaussian beams are given in closed form, making Gaussian beam migration a popular technique for acoustic inversion

[12, 13, 48–51]. Though the goal is to localize scatterers, meaning that the media is *not* weakly scattering, if we only apply one gradient descent step using the imaging condition, then we only need to approximate the Green's function for our initial guess of the slowness m_0. And if m_0 is weakly scattering, the parabolic wave equation serves as a valid approximation [31].

Oftentimes, the initial slowness m_0 is taken to be uniform. However, in our experimental setup, the ocean environment is heterogeneous, and we incorporate this sound speed field information into our initial guess. At each site where we perform acoustic inversion, we measure the sound speed in the ocean column (see figures 4 and 6). Consequently, our best approximation of the environmental media is given by a refractive index (or sound speed or wavenumber) that depends solely on depth: $n^2 = n^2(z)$. In our analysis below, we obtain a closed-form solution to the parabolic wave equation in the form of Gaussian beams in the presence of stratified media.

Consider the narrow-angle parabolic wave equation [41] with the vertical depth chosen as the marching direction,

$$\frac{\partial \psi}{\partial z} = \frac{ik_0}{2}\left(n^2(z) - 1\right)\psi + \frac{i}{2k_0}\left(\frac{\partial^2 \psi}{\partial x^2} + \frac{\partial^2 \psi}{\partial y^2}\right), \qquad (3)$$

where ψ denotes a wave envelope such that the acoustic pressure in the frequency domain is $\hat{p} = e^{ik_0 z}\psi$. Since $n^2 = n^2(z)$, we may Fourier transform in x and y, giving

$$\frac{\partial \tilde{\psi}}{\partial z} = \frac{ik_0}{2}\left(n^2(z) - 1\right)\tilde{\psi} - \frac{i}{2k_0}\left(k_x^2 + k_y^2\right)\tilde{\psi},$$

where $\tilde{}$ denotes the spatial Fourier transform and k_x, k_y are the Fourier dual variables of x, y. Assuming some initial conditions ψ_0 at $z = 0$, this ordinary differential equation is solved by separation of variables.

$$\tilde{\psi}(k_x, k_y, z) = \exp\left(\int_0^z \frac{ik_0}{2}(n^2(s) - 1)ds\right) \cdot \exp\left(-\frac{i}{2k_0}\left(k_x^2 + k_y^2\right)\right)\tilde{\psi}_0$$

Taking the inverse Fourier transform, we obtain

$$\psi(x, y, z) = -\frac{ik_0}{2\pi z}\exp\left(\int_0^z \frac{ik_0}{2}(n^2(s) - 1)ds\right) \cdot \exp\left(\frac{ik_0}{2z}\left(x^2 + y^2\right)\right) * \psi_0(x, y),$$

where $*$ denotes the 2D spatial convolution.

We model the acoustic transmitters (or receivers) as Gaussian sources, first assuming they are aligned in a plane at $z = 0$. We consider the jth transmitter (or receiver) initially, noting that a linear superposition may be taken.

$$\psi_0 = \frac{1}{\sqrt{2\pi\sigma^2}}\exp\left(\frac{(x - x_j)^2 + (y - y_j)^2}{4\sigma^2}\right)$$

Each source is normalized so that its square integral is one. Substituting this into our expression of $\psi(z)$ and multiplying by $\exp(ik_0 z)$ to obtain the pressure field as a sum of Gaussian beams, we have

$$\hat{p}(x, y, z; \omega, x_j, y_j) = \sqrt{\frac{2}{\pi}}\frac{\sigma k_0}{2k_0\sigma^2 + iz}\exp\left(ik_0 z\right) \cdot \exp\left(\frac{ik_0}{2}\int_0^z n^2(s) - 1ds\right) \cdot \exp\left(\frac{-k_0\left((x - x_j)^2 + (y - y_j)^2\right)}{4k_0\sigma^2 + 2iz}\right). \qquad (4)$$

If the sources are located at different values of z, the analysis above may be generalized simply by considering a linear superposition of wave fields. Furthermore, the initial beamwidth is given by $w_0 = 2\sigma$, and the radius of curvature of the beam at $z = 0$ can be modified by changing the complex phase of the initial conditions.

Now, we use our expression for the acoustic pressure $\hat{p}$ in equation (4) to obtain our initial guess $\hat{u}_0$ in equation (1) as well as our adjoint field $\hat{q}$ in equation (2).

$$\hat{u}_0(x, y, z; \omega) = \sum_j \hat{s}_j(\omega)\hat{p}(x, y, z; \omega, x_j^{(s)}, y_j^{(s)}) \qquad (5)$$

$$\hat{q}(x, y, z; \omega) = \sum_j \hat{d}_j(\omega)\hat{p}(x, y, z; \omega, x_j^{(r)}, y_j^{(r)}) \qquad (6)$$

Above, $\hat{s}_j(\omega)$ and $\hat{d}_j(\omega)$ are the acoustic source and receiver signals, respectively, Fourier-transformed in time. The sets $\{x_j^{(s)}, y_j^{(s)}\}_j$ and $\{x_j^{(r)}, y_j^{(r)}\}_j$ are the positions of the transmitters and receivers of the acoustic array. To then obtain a 3D image, we use equations (5) and (6) in the imaging condition (1) and approximate the integral with a discrete sum. With that, we have a closed-form expression to form images in stratified media.

III. Ray-Based Acoustic Inversion

In the following section, we contrast our Gaussian beam migration algorithm with two ray-based approaches: diffraction stack [9] and Kirchhoff migration [10, 11, 14]. Both of these algorithms may be viewed through the lens of the adjoint-state method, making different approximations to the Green's function of the wave equation. Instead of approximating the Green's function with Gaussian beams, a high-frequency ray-based approximation is made.

In both of these methods, an initial guess of uniform slowness is assumed, though curved rays may be incorporated to overcome this [52–54]. The diffraction stack image is then given by

$$\delta m \propto \sum_{j,l} S_{j,l}(x, y, z)d_l(t_0 - \tau_{j,l}(x, y, z)). \qquad (7)$$

The index j corresponds to each transmitter, and the index l corresponds to each receiver. $S_{j,l}$ is a scattering model that takes into account how acoustic pulses reflect off of realistic media both specularly and diffusely [55–57]. The scattering model depends on the receiver-transmitter pair as well as each imaging point (x, y, z) in the 3D domain. t_0 is the starting

time of the transmitted pulse, and $\tau_{j,l}(x,y,z)$ is the traveltime between transmitter j, point (x,y,z), and receiver l.

One formulation of Kirchhoff migration from [11] is given by

$$\delta m \propto \sum_{j,l} S_{j,l}(x,y,z)(\cos\phi_j(x,y,z) + \cos\phi_l(x,y,z))\cdot \frac{d}{dt} d_l(t_0 - \tau_{j,l}(x,y,z)), \quad (8)$$

where $\phi_j(x,y,z)$ is the angle between the vertical and the line connecting transmitter j and the point (x,y,z) while ϕ_l is the angle between the vertical and the line connecting receiver l and the point (x,y,z). The cosine terms and derivative arise from the exploding reflector model, but kinematically, equations (7) and (8) are the same: energy will be placed at the same locations, but there may be more artifacts in one algorithm compared to the other. In both algorithms, $\tau_{j,l}(x,y,z)$ is computed as the distance between transmitter j and point (x,y,z) plus the distance between point (x,y,z) and receiver l divided by the (uniform) sound speed.

IV. Algorithmic Comparison

A. Validation Using Simulated Data

To compare the three algorithms, we need to know the ground truth. With data gathered by our acoustic array in the ocean, the true bathymetry and objects in the ocean are unknown. Furthermore, environmental noise pollutes the data, making a comparison challenging. So, we used simulated data from diverse numerical configurations to determine which algorithm produces the best and cleanest image. Here, we report the results of one such configuration. We define a 2D computational domain with $x \in [-.75, .75]$ and $z \in [0, 1.05]$ with uniform sound speed $c = 1{,}500$ m/s. We place nine co-located receivers and transmitters at $x = [-0.53492, -0.5, -0.41413, -0.11914, -0.042327, 0, 0.41402, 0.5, 0.601]$ and $z = 0$. Then, we generate the bathymetry $b(x)$ using a linear superposition of Gaussians.

$$b(x) = 0.99875 - 0.05 * \exp\left(-\frac{x^2}{.02}\right) - 0.025 * \exp\left(-\frac{(x-0.2)^2}{.0005}\right) - 0.04 * \exp\left(-\frac{(x+0.4)^2}{0.0025}\right)$$

Finally, we assume each transmitter j emits a Gaussian pulse of the form

$$\psi_0(x) = \exp\left(\frac{(x - x_j^s)^2}{2 \cdot 10^{-5}}\right).$$

To obtain the full wavefield in the domain, we use a coupled numerical solver comprised of a parabolic wave equation solver and a Helmholtz equation solver. The narrow-angle parabolic wave equation (3) is valid in weakly scattering media, i.e. the area above the bathymetry. The Helmholtz equation is valid everywhere, but since it is an elliptic rather than a parabolic PDE, it is more expensive to compute. So, we solve the narrow-angle parabolic wave equation from $z = 0$ to $z = 1.05$ via the split-step Fourier algorithm with an artificial absorption layer in x [42]. Next, we solve the Helmholtz equation in a small region at the bottom of the domain using the method of fundamental solutions [58], setting the pressure to be the additive inverse of the parabolic wave equation solution at the bathymetry. In doing so, we can add the two fields, and a Dirichlet-zero condition will be enforced at the bathymetry. Finally, the narrow-angle parabolic wave equation is solved again, this time from the bottom up, to propagate scattered energy back to the receivers. The initial conditions for the final parabolic wave equation solve are taken to be a slice of the acoustic field obtained from the Helmholtz equation above the bathymetry. Note that we do not include the solution from the initial parabolic wave equation in the initial conditions for the final parabolic wave equation solve since that solution corresponds to downward-propagating energy. The full wavefield is given by the superposition of each numerical solution in its respective domain. This entire process is repeated for 501 frequencies from 0 Hz to 150,000 Hz with a frequency spacing of 300 Hz. Once completed, data at only the receivers are stored and inverted back into the time domain via the inverse discrete Fourier transform.

The results of applying each imaging algorithm to the

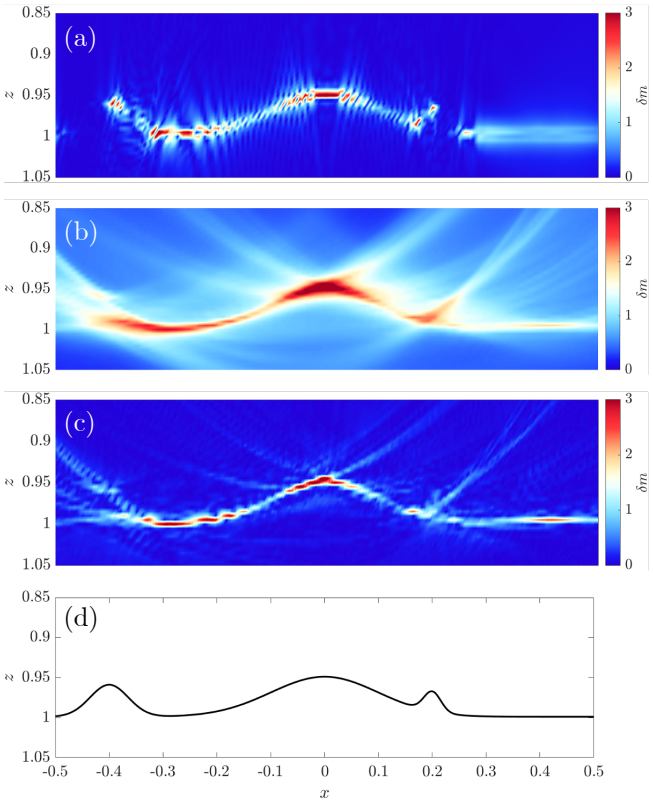

Fig. 1. 2D simulated results. We compute images, i.e. the model perturbation δm, using (a) Gaussian beam migration, (b) diffraction stack, and (c) Kirchhoff migration. In (d), we show the ground truth.

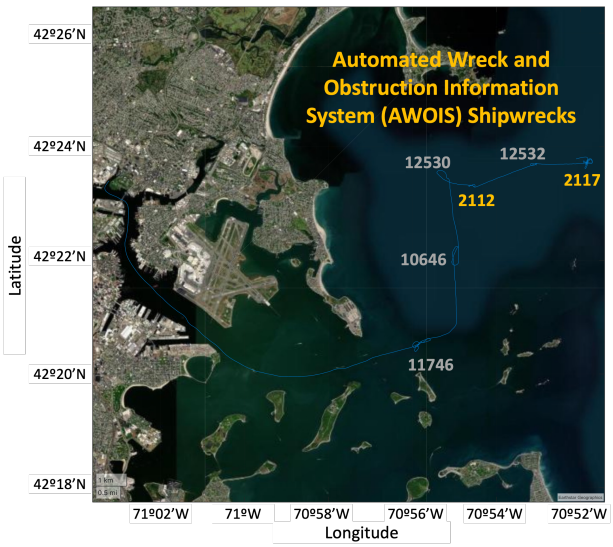

Fig. 2. Sea test route and shipwreck identifiers.

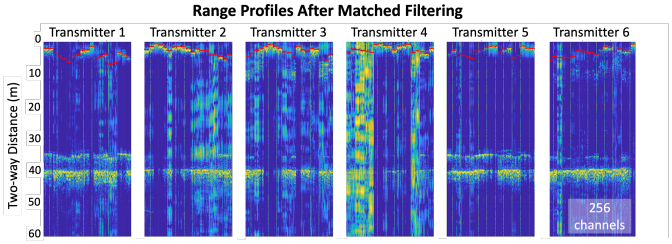

(a) AWOIS 2112

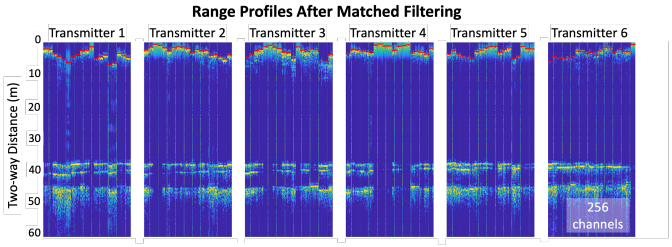

(b) AWOIS 2117

Fig. 3. AWOIS 2112 and AWOIS 2117 range profiles of all transmit–receive pairs after matched filtering.

simulated data, i.e. computing the three model perturbations δm_{GBM}, δm_{DS}, and δm_{KM}, are shown in Figure 1. Our new Gaussian beam migration (GBM) produces the sharpest image with the fewest artifacts. Diffraction stack (DS) produces a smeared image as it does not include amplitude corrections to the imaging condition. Kirchhoff migration (KM) is less smeared and more similar to Gaussian beam migration; however, it includes hyperbolic artifacts. In each case, the right side of the small Gaussian bump at $x = 0.2$ is not captured because reflections off of that steep side are not recorded by the fictitious hydrophone array. Increasing the number of transmitters and receivers would recover the full bathymetry.

B. Evaluation using Ocean Array Data

Next, we compare the techniques with real data we collected during two ocean tests using a custom-built large sparse aperture sonar array operating at 33 kHz. More information about the array and the tests can be found in [8]. Figure 2 shows the sea test route along with shipwreck identifiers based on the Automated Wreck and Obstruction Information System (AWOIS) records [59]. In this paper, the data collected from imaging the AWOIS 2112 (collected during sea test 2 on May 19, 2021) and 2117 (collected during sea test 1 on October 9, 2020) sites are used for showcasing our closed-form Gaussian beam migration algorithm.

Starting with the AWOIS 2112 site located at (42.39°N, -70.92°W), the data we collected consists of navigation data from a dual antenna inertial navigation system, sound speed profiles, and the array data obtained using 6 transmitters and 256 receivers. The array data was first health checked for faulty channels and then matched filtered. Following that, we time-aligned the data across all receive channels and calibrated for the array positions using the navigation data. The matched filtered and calibrated data collected at AWOIS 2112 is shown

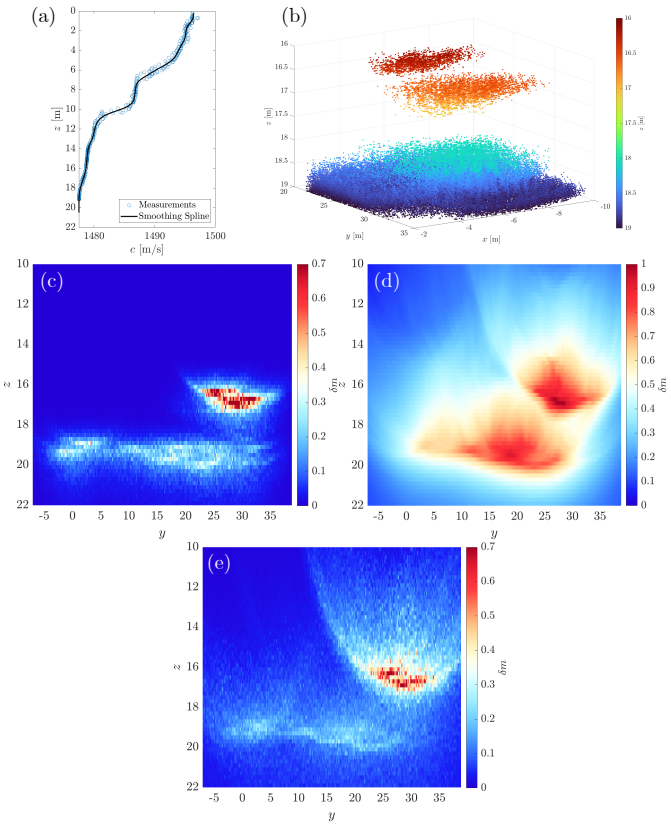

Fig. 4. AWOIS 2112 sound speed profiles and images from May 19, 2021. (a) Measured sound speed and smoothing spline fit to the measurements. (b) 3D point cloud of the acoustic scatterers. Below, we show 2D slices obtained by taking the maximum energy over the x dimension using (c) Gaussian beam migration, (d) diffraction stack, and (e) Kirchhoff migration.

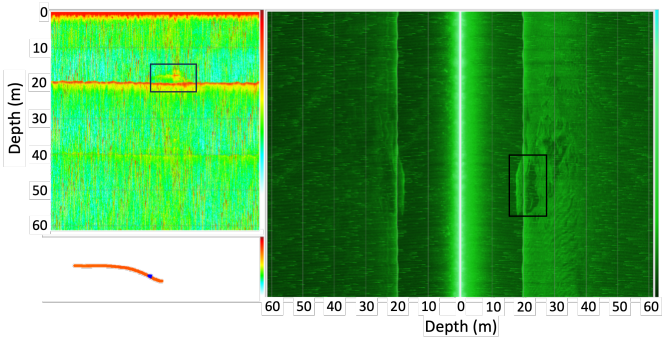

Fig. 5. Reference imagery of the seabed at the AWOIS 2112 site obtained on May 19, 2021 using a Humminbird Helix 7 side-scan sonar operating at 462 kHz. The black box highlights the identified sunken object.

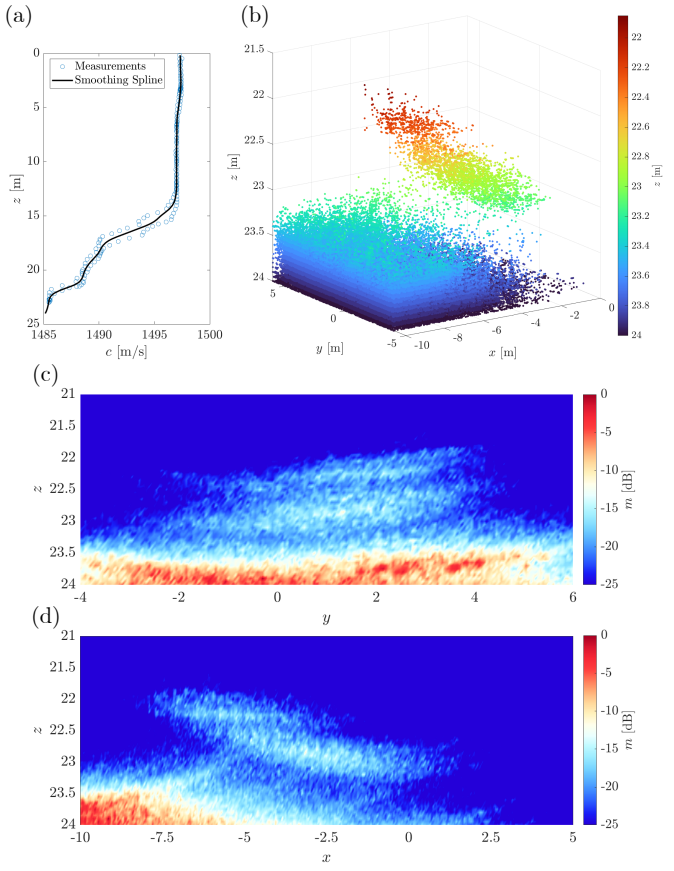

Fig. 6. AWOIS 2117 sound speed profiles and images from October 9, 2020. (a) Measured sound speed and smoothing spline fit to the measurements. (b) 3D point cloud obtained with Gaussian beam migration. (c) and (d) Different 2D slices by taking the maximum energy over x and y, respectively.

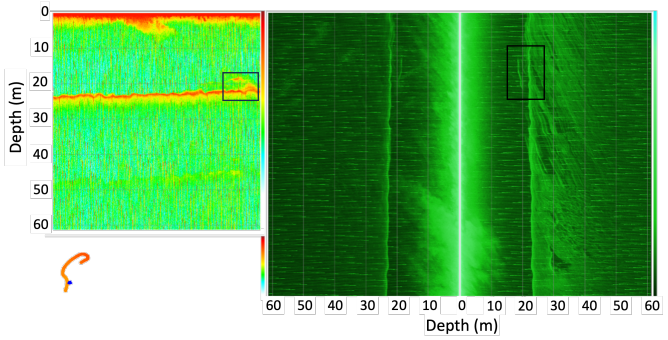

Fig. 7. Reference imagery of the seabed at the AWOIS 2117 site obtained on October 9, 2020 using a Humminbird Helix 7 side-scan sonar operating at 462 kHz. The black box highlights the identified sunken object.

in Figure 3a, where time signals are plotted as the two-way distance range profiles, i.e. the distance it takes for the signal to travel from the transmitter, propagate, and scatter through the medium, then travel back to the receiver. In this figure, the direct blasts (highlighted in red) and surface and bottom reflections can be seen. This data was then used in our imaging algorithms. Our Gaussian beam migration code accounts for the measured sound speed profile at that location (shown in panel (a) in Figure 4), while our implementation of diffraction stack and Kirchhoff migration, however, does not take this profile into account and assumes a constant sound speed in the medium.

In Figure 4, we show a 3D point cloud of the image as well as 2D slices of the image. In addition to measuring the bathymetry, we image what appears to be two objects above the seafloor. In this realistic case, the Gaussian beam migration algorithm again produces the cleanest image, while diffraction stack smears the image, and Kirchhoff migration introduces hyperbolic artifacts. These maps can be compared to a reference imagery of the seabed we collected during our sea test using a Humminbird Helix 7 side-scan sonar operating at 462 kHz. The reference imagery is provided in figure 5 with the identified sunken object highlighted by the black box. Comparing the reference map to our sparse aperture array images obtained using the closed-form Gaussian beam migration algorithm, we see that our algorithm successfully migrates the image to the correct depth and provides an image resolution comparable to the side-scan sonar image while operating at a much lower (around 14x lower) frequency.

Finally, we show the data and results from the AWOIS 2117 site located at 42.39°N, -70.86°W. In figure 3b, we show the range profiles of the array data. Figure 6 shows the sound speed profile and the 3D point cloud from the Gaussian beam migration. We also show 2D slices of the 3D image. Though a majority of the energy received is reflected off of the bathymetry, there is clearly an object resting on the seafloor. Comparing our sparse aperture array images to the reference imagery obtained using a Humminbird Helix 7 side-scan sonar shown in figure 7, the sunken object in the migrated image is placed at the correct depth with comparable image resolution.

V. Conclusion

From the imaging condition, we derived a closed-form expression for Gaussian beam migration in stratified media and compared the formulation with diffraction stack and Kirchhoff migration. Through numerical simulation and realistic test cases with data collected over shipwrecks in the Boston Harbor, we have shown the improved efficacy of Gaussian beam migration over diffraction stack and Kirchhoff migration. Images produced by Gaussian beam migration are sharp and minimize hyperbolic artifacts present in ray-based methods. In addition, we demonstrated how our large sparse aperture sonar array and our closed-form Gaussian beam migration algorithm can generate seafloor maps at a comparable resolution to a commercial high-frequency side-scan sonar.

To accelerate the imaging computation, we parallelized our algorithms and ran them on GPUs. For Gaussian beam migration in particular, the image formation may be embarrassingly parallelized in two ways. First, an image may be constructed for each transmitter separately on individual processors and summed at the end. Second, the integrand (or discrete sumand) in (1) may be parallelized over frequency. Furthermore, the entire frequency domain need not be utilized; we use a bandpass filter with frequency cutoffs computed at user-defined thresholds of the source spectrum. Diffraction stack and Kirchhoff migration may be parallelized over each voxel/point in the domain. After parallelizing and porting our Gaussian beam migration code to GPUs, we saw a $> 450\times$ speedup.

In the future, we hope to incorporate scattering models [55–57] and advanced imaging conditions [60, 61] into the Gaussian beam migration in an effort to further improve image clarity. Additionally, we hope to develop more robust post-processing techniques to recognize discrete objects and further reduce any remaining imaging artifacts. Finally, we intend to perform a sensitivity analysis and incorporate Bayesian inversion and uncertainty quantification [62–65]. This would allow us to understand how uncertainty in the environment, as well as stochasticity in the transmitter/receiver locations, angles, and source signals, affect the resulting image. This future direction can build upon our recent work on developing stochastic reduced-order models that capture the probability density function of acoustic waves propagating in a stochastic environment using the Dynamically Orthogonal Parabolic Equations [66–68].

Acknowledgment

The authors would like to thank the MSEAS group members for their contributions. We thank the MIT Lincoln Laboratory Autonomous Systems Line and Integrated Systems Line for their generous support of this work.

DISTRIBUTION STATEMENT A.

Approved for public release. Distribution is unlimited. This material is based upon work supported by the Under Secretary of Defense for Research and Engineering under Air Force Contract No. FA8702-15-D-0001. Any opinions, findings, conclusions or recommendations expressed in this material are those of the author(s) and do not necessarily reflect the views of the Under Secretary of Defense for Research and Engineering.

References

[1] T. A. Kearns and J. Breman, "Bathymetry-the art and science of seafloor modeling for modern applications," *Ocean globe*, pp. 1–36, 2010.

[2] R. E. Hansen, H. J. Callow, T. O. Sabo, and S. A. V. Synnes, "Challenges in seafloor imaging and mapping with synthetic aperture sonar," *IEEE Transactions on geoscience and Remote Sensing*, vol. 49, no. 10, pp. 3677–3687, 2011.

[3] L. A. Levin, B. J. Bett, A. R. Gates, P. Heimbach, B. M. Howe, F. Janssen, A. McCurdy, H. A. Ruhl, P. Snelgrove, K. I. Stocks, D. Bailey, S. Baumann-Pickering, C. Beaverson, M. C. Benfield, D. J. Booth, M. Carreiro-Silva, A. Colaço, M. C. Eblé, A. M. Fowler, K. M. Gjerde, D. O. B. Jones, K. Katsumata, D. Kelley, N. Le Bris, A. P. Leonardi, F. Lejzerowicz, P. I. Macreadie, D. McLean, F. Meitz, T. Morato, A. Netburn, J. Pawlowski, C. R. Smith, S. Sun, H. Uchida, M. F. Vardaro, R. Venkatesan, and R. A. Weller, "Global observing needs in the deep ocean," *Frontiers in Marine Science*, vol. 6, 2019.

[4] A.-C. Wölfl, H. Snaith, S. Amirebrahimi, C. W. Devey, B. Dorschel, V. Ferrini, V. A. I. Huvenne, M. Jakobsson, J. Jencks, G. Johnston, G. Lamarche, L. Mayer, D. Millar, T. H. Pedersen, K. Picard, A. Reitz, T. Schmitt, M. Visbeck, P. Weatherall, and R. Wigley, "Seafloor mapping – the challenge of a truly global ocean bathymetry," *Frontiers in Marine Science*, vol. 6, 2019.

[5] A. M. Rengstorf, C. Mohn, C. Brown, M. S. Wisz, and A. J. Grehan, "Predicting the distribution of deep-sea vulnerable marine ecosystems using high-resolution data: Considerations and novel approaches," *Deep Sea Research Part I: Oceanographic Research Papers*, vol. 93, pp. 72–82, 2014.

[6] K. Picard, B. P. Brooke, P. T. Harris, P. J. Siwabessy, M. F. Coffin, M. Tran, M. Spinoccia, J. Weales, M. Macmillan-Lawler, and J. Sullivan, "Malaysia airlines flight mh370 search data reveal geomorphology and seafloor processes in the remote southeast indian ocean," *Marine Geology*, vol. 395, pp. 301–319, 2018.

[7] F. L. Chiocci, A. Cattaneo, and R. Urgeles, "Seafloor mapping for geohazard assessment: state of the art," *Marine Geophysical Research*, vol. 32, no. 1, pp. 1–11, 2011.

[8] P. Ryu, D. Brown, K. Arsenault, B. Cho, A. March, W. H. Ali, A. Charous, and P. F. J. Lermusiaux, "A wide-area deep ocean floor mapping system: Design and sea tests," *Geomatics*, vol. 3, no. 1, pp. 290–311, Mar. 2023, special issue "Advances in Ocean Mapping and Nautical Cartography".

[9] W. S. French, "Two-dimensional and three-dimensional migration of model-experiment reflection profiles," *Geophysics*, vol. 39, no. 3, pp. 265–277, 1974.

[10] W. A. Schneider, "Integral formulation for migration in two and three dimensions," *Geophysics*, vol. 43, no. 1, pp. 49–76, 1978.

[11] X. Zhuge, T. Savelyev, A. G. Yarovoy, and L. Ligthart, "Uwb array-based radar imaging using modified kirchhoff migration," in *2008 IEEE International Conference on Ultra-Wideband*, vol. 3. IEEE, 2008, pp. 175–178.

[12] N. R. Hill, "Gaussian beam migration," *Geophysics*, vol. 55, no. 11, pp. 1416–1428, 1990.

[13] ——, "Prestack gaussian-beam depth migration," *Geophysics*, vol. 66, no. 4, pp. 1240–1250, 2001.

[14] Ö. Yilmaz, *Seismic data analysis*. Society of exploration geophysicists Tulsa, 2001, vol. 1.

[15] E. Baysal, D. D. Kosloff, and J. W. C. Sherwood, "Reverse time migration," *GEOPHYSICS*, vol. 48, no. 11, pp. 1514–1524, 1983. [Online]. Available: https://doi.org/10.1190/1.1441434

[16] J. F. Claerbout, *Imaging the earth's interior*. Blackwell scientific publications Oxford, 1985, vol. 1.

[17] A. Tarantola, "Inversion of seismic reflection data in the acoustic approximation," *GEOPHYSICS*, vol. 49, no. 8, pp. 1259–1266, 1984. [Online]. Available: https://doi.org/10.1190/1.1441754

[18] R.-E. Plessix, "A review of the adjoint-state method for computing the gradient of a functional with geophysical applications," *Geophysical Journal International*, vol. 167, no. 2, pp. 495–503, 2006.

[19] W. W. Symes, "Reverse time migration with optimal checkpointing," *GEOPHYSICS*, vol. 72, no. 5, pp. SM213–SM221, 2007. [Online]. Available: https://doi.org/10.1190/1.2742686

[20] D. Colton and R. Kress, *Integral equation methods in scattering theory*. SIAM, 2013.

[21] D. Roy and L. S. Couchman, *Inverse problems and inverse scattering of plane waves*. Academic Press, 2001.

[22] A. Fichtner, H.-P. Bunge, and H. Igel, "The adjoint method in seismology: I. theory," *Physics of the Earth and Planetary Interiors*, vol. 157, no. 1, pp. 86–104, 2006. [Online]. Available: https://www.sciencedirect.com/science/article/pii/S0031920106001051

[23] A. Devaney, "Diffraction tomography," in *Inverse Methods in Electromagnetic Imaging: Part 2*. Springer, 1985, pp. 1107–1135.

[24] D. L. Colton, R. Kress, and R. Kress, *Inverse acoustic and electromagnetic scattering theory*. Springer, 1998, vol. 93.

[25] C. Wunsch, *The Ocean Circulation Inverse Problem*. Cambridge University Press, 1996.

[26] A. F. Bennett, *Inverse Methods in Physical Oceanography*, ser. Cambridge Monographs on Mechanics. Cambridge University Press, 1992.

[27] C. Pires and P. M. Miranda, "Tsunami waveform inversion by adjoint methods," *Journal of Geophysical Research: Oceans*, vol. 106, no. C9, pp. 19 773–19 796, 2001.

[28] M. C. G. Hall and D. G. Cacuci, "Physical interpretation of the adjoint functions for sensitivity analysis of atmospheric models," *Journal of Atmospheric Sciences*, vol. 40, no. 10, pp. 2537 – 2546, 1983. [Online]. Available: https://journals.ametsoc.org/view/journals/atsc/40/10/1520-0469_1983_040_2537_piotaf_2_0_co_2.xml

[29] O. Talagrand, "Application of optimal control to meteorological problems," in *Variational Methods in Geosciences*, ser. Developments in Geomathematics, Y. K. Sasaki, Ed. Elsevier, 1986, vol. 5, pp. 13–28. [Online]. Available: https://www.sciencedirect.com/science/article/pii/B9780444426970500084

[30] R. M. Errico, "What is an adjoint model?" *Bulletin of the American Meteorological Society*, vol. 78, no. 11, pp. 2577–2592, 1997.

[31] P. Hursky, M. B. Porter, B. D. Cornuelle, W. S. Hodgkiss, and W. A. Kuperman, "Adjoint modeling for acoustic inversion," *The Journal of the Acoustical Society of America*, vol. 115, no. 2, pp. 607–619, 01 2004. [Online]. Available: https://doi.org/10.1121/1.1636760

[32] A. Thode, "The derivative of a waveguide acoustic field with respect to a three-dimensional sound speed perturbation," *The Journal of the Acoustical Society of America*, vol. 115, no. 6, pp. 2824–2833, 06 2004. [Online]. Available: https://doi.org/10.1121/1.1736651

[33] J.-L. Li, L.-L. Jin, and W. Xu, "Inversion of internal wave-perturbed sound-speed field via acoustic data assimilation," *IEEE Journal of Oceanic Engineering*, vol. 39, no. 3, pp. 407–418, 2014.

[34] M. Meyer and J.-P. Hermand, "Backpropagation techniques in ocean acoustic inversion: time reversal, retrogation and adjoint model–a review," *Acoustic Sensing Techniques for the Shallow Water Environment: Inversion methods and experiments*, pp. 29–46, 2006.

[35] J.-P. Hermand, M. Meyer, M. Asch, and M. Berrada, "Adjoint-based acoustic inversion for the physical characterization of a shallow water environmenta)," *The Journal of the Acoustical Society of America*, vol. 119, no. 6, pp. 3860–3871, 06 2006. [Online]. Available: https://doi.org/10.1121/1.2197790

[36] F. Badran, M. Berrada, J. Brajard, M. Crépon, C. Sorror, S. Thiria, J.-P. Hermand, M. Meyer, L. Perichon, and M. Asch, "Inversion of satellite ocean colour imagery and geoacoustic characterization of seabed properties: Variational data inversion using a semi-automatic adjoint approach," *Journal of Marine Systems*, vol. 69, no. 1, pp. 126–136, 2008,

maritime Rapid Environmental Assessment. [Online]. Available: https://www.sciencedirect.com/science/article/pii/S0924796307000401

[37] J. S. Papadakis and E. Karasmani, "Gradient of the cost function via the adjoint method for underwater acoustic inversion," *Journal of Theoretical and Computational Acoustics*, vol. 28, no. 01, p. 1950010, 2020. [Online]. Available: https://doi.org/10.1142/S2591728519500105

[38] M. Meyer, J.-P. Hermand, M. Asch, and J.-C. L. Gac, "An analytic multiple frequency adjoint-based inversion algorithm for parabolic-type approximations in ocean acoustics," *Inverse Problems in Science and Engineering*, vol. 14, no. 3, pp. 245–265, 2006. [Online]. Available: https://doi.org/10.1080/17415970500408023

[39] M. Meyer, J.-P. Hermand, M. Berrada, and M. Asch, "Remote sensing of tyrrhenian shallow waters using the adjoint of a full-field acoustic propagation model," *Journal of marine systems*, vol. 78, pp. S339–S348, 2009.

[40] L. Demanet, "Waves and imaging," 2021.

[41] F. D. Tappert, "The parabolic approximation method," in *Wave Propagation and Underwater Acoustics*, ser. Lecture Notes in Physics, Berlin Springer Verlag, J. B. Keller and J. S. Papadakis, Eds., vol. 70, 1977, p. 224.

[42] F. B. Jensen, W. A. Kuperman, M. B. Porter, and H. Schmidt, *Computational Ocean Acoustics*. Springer Science & Business Media, 2011.

[43] M. Cheney and B. Borden, *Fundamentals of radar imaging*. SIAM, 2009.

[44] V. Červenỳ, M. M. Popov, and I. Pšenčík, "Computation of wave fields in inhomogeneous media—gaussian beam approach," *Geophysical Journal International*, vol. 70, no. 1, pp. 109–128, 1982.

[45] M. M. Popov, "A new method of computation of wave fields using gaussian beams," *Wave motion*, vol. 4, no. 1, pp. 85–97, 1982.

[46] V. Červenỳ and I. Pšenčík, "Gaussian beams in two-dimensional elastic inhomogeneous media," *Geophysical Journal International*, vol. 72, no. 2, pp. 417–433, 1983.

[47] A. Kiselev, "Modulated gaussian beams," *Radiophysics and Quantum Electronics*, vol. 26, no. 8, pp. 755–761, 1983.

[48] S. H. Gray, "Gaussian beam migration of common-shot records," *Geophysics*, vol. 70, no. 4, pp. S71–S77, 2005.

[49] S. H. Gray and N. Bleistein, "True-amplitude gaussian-beam migration," *Geophysics*, vol. 74, no. 2, pp. S11–S23, 2009.

[50] H. Hu, Y. Liu, Y. Zheng, X. Liu, and H. Lu, "Least-squares gaussian beam migration," *Geophysics*, vol. 81, no. 3, pp. S87–S100, 2016.

[51] J. Yang, H. Zhu, G. McMechan, and Y. Yue, "Time-domain least-squares migration using the gaussian beam summation method," *Geophysical Journal International*, vol. 214, no. 1, pp. 548–572, 2018.

[52] J. A. Carter and L. N. Frazer, "Accommodating lateral velocity changes in kirchhoff migration by means of fermat's principle," *Geophysics*, vol. 49, no. 1, pp. 46–53, 1984.

[53] S. H. Gray, "Efficient traveltime calculations for kirchhoff migration," *Geophysics*, vol. 51, no. 8, pp. 1685–1688, 1986.

[54] S. H. Gray and W. P. May, "Kirchhoff migration using eikonal equation traveltimes," *Geophysics*, vol. 59, no. 5, pp. 810–817, 1994.

[55] R. J. Urick, *Principles of Underwater Sound*. New York: McGraw-Hill, 423 pp., 1976.

[56] B. T. Phong, "Illumination for computer generated pictures," *Communications of the ACM*, vol. 18, no. 6, pp. 311–317, 1975.

[57] D. D. Ellis and D. V. Crowe, "Bistatic reverberation calculations using a three-dimensional scattering function," *The Journal of the Acoustical Society of America*, vol. 89, no. 5, pp. 2207–2214, 1991.

[58] G. Fairweather, A. Karageorghis, and P. A. Martin, "The method of fundamental solutions for scattering and radiation problems," *Engineering analysis with boundary elements*, vol. 27, no. 7, pp. 759–769, 2003.

[59] Office of Coast Survey, "Office of coast survey's Automated Wreck and Obstruction Information System (AWOIS)," NOAA National Centers for Environmental Information, 2023. [Online]. Available: https://www.fisheries.noaa.gov/inport/item/39988

[60] F. Liu, G. Zhang, S. A. Morton, and J. P. Leveille, "An effective imaging condition for reverse-time migration using wavefield decomposition," *GEOPHYSICS*, vol. 76, no. 1, pp. S29–S39, 2011. [Online]. Available: https://doi.org/10.1190/1.3533914

[61] S. Greer and L. Demanet, "Superresolution with the zero-phase imaging condition," *arXiv preprint arXiv:2304.01013*, 2023.

[62] P. F. J. Lermusiaux, "Uncertainty estimation and prediction for interdisciplinary ocean dynamics," *Journal of Computational Physics*, vol. 217, no. 1, pp. 176–199, 2006.

[63] P. F. J. Lermusiaux, C.-S. Chiu, G. G. Gawarkiewicz, P. Abbot, A. R. Robinson, R. N. Miller, P. J. Haley, Jr, W. G. Leslie, S. J. Majumdar, A. Pang, and F. Lekien, "Quantifying uncertainties in ocean predictions," *Oceanography*, vol. 19, no. 1, pp. 92–105, 2006.

[64] P. F. J. Lermusiaux, C. Mirabito, P. J. Haley, Jr., W. H. Ali, A. Gupta, S. Jana, E. Dorfman, A. Laferriere, A. Kofford, G. Shepard, M. Goldsmith, K. Heaney, E. Coelho, J. Boyle, J. Murray, L. Freitag, and A. Morozov, "Real-time probabilistic coupled ocean physics-acoustics forecasting and data assimilation for underwater GPS," in *OCEANS 2020 IEEE/MTS*. IEEE, Oct. 2020, pp. 1–9.

[65] P. F. J. Lermusiaux, P. J. Haley, Jr., C. Mirabito, W. H. Ali, M. Bhabra, P. Abbot, C.-S. Chiu, and C. Emerson, "Multi-resolution probabilistic ocean physics-acoustic modeling: Validation in the New Jersey continental shelf," in *OCEANS 2020 IEEE/MTS*. IEEE, Oct. 2020, pp. 1–9.

[66] W. H. Ali, M. S. Bhabra, P. F. J. Lermusiaux, A. March, J. R. Edwards, K. Rimpau, and P. Ryu, "Stochastic oceanographic-acoustic prediction and Bayesian inversion for wide area ocean floor mapping," in *OCEANS 2019 MTS/IEEE SEATTLE*. Seattle: IEEE, Oct. 2019, pp. 1–10.

[67] W. H. Ali and P. F. J. Lermusiaux, "Dynamically orthogonal narrow-angle parabolic equations for stochastic underwater sound propagation," *Journal of the Acoustical Society of America*, 2023, sub-judice.

[68] ——, "Dynamically orthogonal wide-angle parabolic equations for stochastic underwater sound propagation," *Journal of the Acoustical Society of America*, 2023, in preparation.